Supporting Information: Phonon-mediated ultrafast dynamics in self-assembled monolayers of 4-mercaptobenzoic acid on gold

Savini Bandaranayake,[†] Paul Schrader,[†] Guangzhao Chen,[‡] Liang Z. Tan,[‡] Mohana Shivanna,[†] Vitalie Stavila,[†] Juan R. Luna,[¶] and Krupa Ramasesha[*,†]

†*Sandia National Laboratories, Livermore, California 94550, USA*

‡*Molecular Foundry, Lawrence Berkeley National Laboratory, Berkeley, California 94720, USA*

¶*Department of Chemistry and Biochemistry, The University of Texas at El Paso, El Paso, USA*

E-mail: kramase@sandia.gov

Contents

S1. HOMO and LUMO orbital images of 4MBA and 4MBA-Au

Figure S1: HOMO (left) and LUMO (right) orbital states of the isolated 4MBA system.

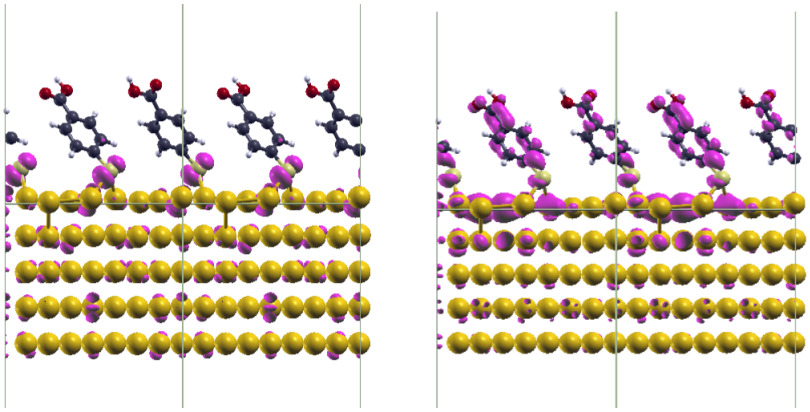

Figure S2: Representative HOMO (left) and LUMO (right) orbital states of 4MBA-Au system. The HOMO state selected was located -0.505 eV below the Fermi level. The LUMO state selected was located 2.246 eV above the Fermi level.

Orbital images of the HOMO and the LUMO of an isolated 4MBA molecule and 4MBA-Au obtained from ground-state DFT calculations are shown in Figures S1 and S2, respectively. The HOMO of the 4MBA molecule is mainly localized on the sulfur atom along with some weight on the aromatic carbons in close proximity to the sulfur atom. The LUMO is

delocalized across the entire aromatic ring and the -COOH functional group. Orbitals of the 4MBA-Au show delocalization similar to what is observed in 4MBA molecule, but now with orbital delocalization extending into the Au lattice in both HOMO and LUMO.

S2. 4MBA-Au phonon mode calculation

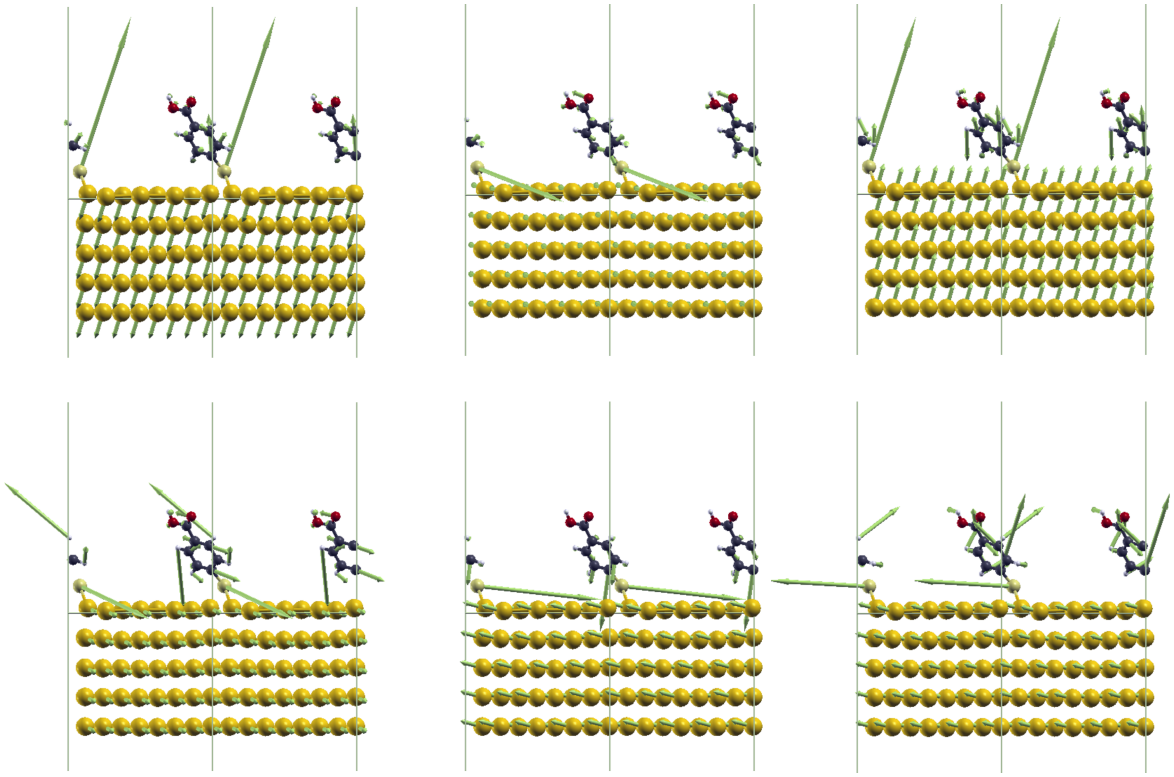

Figure S3: Acoustic phonon modes of 4MBA-Au system showing strong hybridization between Au acoustic modes and molecular vibration modes containing sulfur. Arrows denote magnitude of phonon displacement.

To compute the vibrational modes of isolated 4MBA, we used density functional perturbation theory (DFPT) as implemented in the Quantum Espresso software package.[1] The simulation cell, containing one isolated 4MBA molecule, had dimensions of 5.12Å×11.8Å×10.0Å, chosen to be commensurate with the 4MBA-Au system in the directions parallel to the Au surface. Geometry optimization and DFPT calculations were performed in a planewave basis set with cutoff kinetic energy of 60 Ry, utilizing norm-conserving pseudopotentials and the

PBE exchange-correlation functional. Geometry optimization used force and energy convergence thresholds of 10^{-3} and 10^{-4} (atomic units), respectively. We obtained the dynamical matrix for the isolated 4MBA system, from which the vibrational eigenmodes and frequencies were computed.

To circumvent the computational cost of calculating acoustic phonon modes in the large 4MBA-Au system, we parameterized harmonic force constants using a frozen-phonon approach within density functional theory. For the phonon calculations of 4MBA-Au, we use a slab model with only one 4MBA molecule per unit cell. The geometry of this slab model was optimized to force and energy convergence thresholds of 10^{-3} and 10^{-4} (atomic units) respectively. The 4MBA molecule of the 4MBA-Au system was displaced according to each vibrational eigenmode of the isolated 4MBA. For each of these eigenmodes, 6 displacement amplitudes ranging from -0.3Åto +0.3Å(cumulative over all 4MBA atoms) were considered. For each of these displacement patterns, the DFT force on all of the 4MBA-Au atoms was computed. A linear fit of the DFT force-vs-displacement data was performed to obtain harmonic force constants of the 4MBA-Au system. We construct a reduced dynamical matrix using the basis of the isolated 4MBA vibrational eigenmodes together with three acoustic Au modes. The acoustic Au modes are taken as homogeneous displacement patterns of all Au atoms in x,y,z directions. The reduced dynamical matrix is obtained from the force constants matrix using the equation $D_{\mu\nu} = \sum_{ij} U_{\mu i}(C_{ij}/\sqrt{m_i m_j})U^*_{\nu j}$, where $U_{\mu i}$ is the matrix of eigenmode basis vectors for mode μ and atomic degree of freedom $i = (\alpha_i, \tau_i)$, corresponding to atom α_i with displacement in cartesian direction τ_i. Here, m_i is the mass of atom α_i. The force constants matrix C_{ij} was obtained from the frozen phonon method as described above. Diagonalizing the reduced density matrix $D_{\mu\nu}$ results in the acoustic phonon modes of the combined 4MBA-Au system.

S3. Characterization of the 4MBA-Au sample after laser exposure

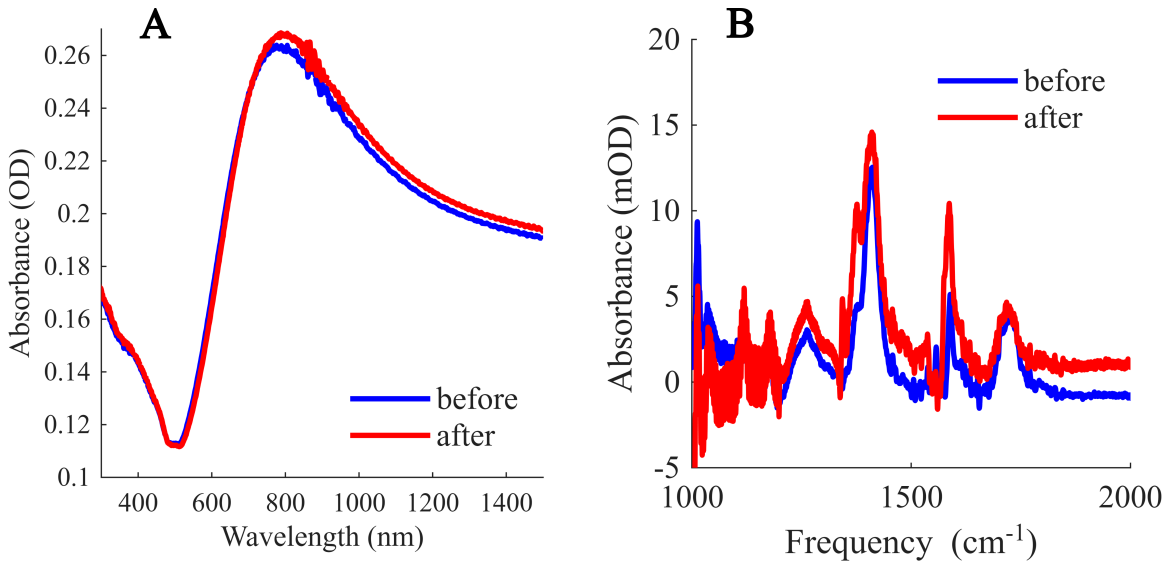

Figure S4: A) Static UV-visible spectra and B) FTIR spectra of 4MBA-Au sample before (blue) and after (red) exposing the sample to WLC and 50 μJ/cm^2 pump.

Damage threshold studies were performed on Au and 4MBA-Au to check the stability of samples against ultrafast laser irradiation. Static UV-visible and FT-IR measurements were performed on 4MBA-Au samples before and after exposure to the pump and probe at a fixed time delay while continuously rastering the sample to observe any pump and/or probe induced changes to samples. Figure S4 shows the static UV-visible and FTIR spectra of a 4MBA-Au sample before and after exposing the sample to laser irradiation for 9 hours at a pump fluence of 50 μJ cm^{-2}. Minimal changes in the static UV-visible absorption spectra before and after laser exposure is indicative of the nanostructure of Au remaining largely unchanged. The presence of signatures of 4MBA vibrational modes indicates that the chosen laser fluence is insufficient to induce desorption. However, the changes in the FTIR baseline after laser exposure could indicate minor structural modifications in Au, which changes the tail of the Au plasmon resonance that extends to the mid-infrared region.[2,3] We also observe a relative intensity change of the two peaks in the IR doublet at 1415 cm^{-1} after laser

irradiation. This can arise from changes in the coupling between vibrational modes due to modifications in the Au plasmon resonance band and/or permanent conformational changes induced by higher lattice temperatures, although the other IR signatures remain unchanged suggesting that the latter possibility is not likely. We note that the relative intensity in the feature at 1415 cm^{-1} remains unchanged after exposing the sample to the pump and probe for a few hours. During this time, the full sample is exposed to both beams multiple times, and we can assume that the sample has reached its new equilibrium state by this time. Comparative TA measurements were performed on samples that had reached this new equilibrium. We also used higher pump fluences (100 and 150 μJ cm^{-2}) and observed only minor changes in steady-state UV-visible and FTIR spectra indicating that the 4MBA-Au samples are robust against the fluences used in this work.

S4. TAS data for an additional set of samples

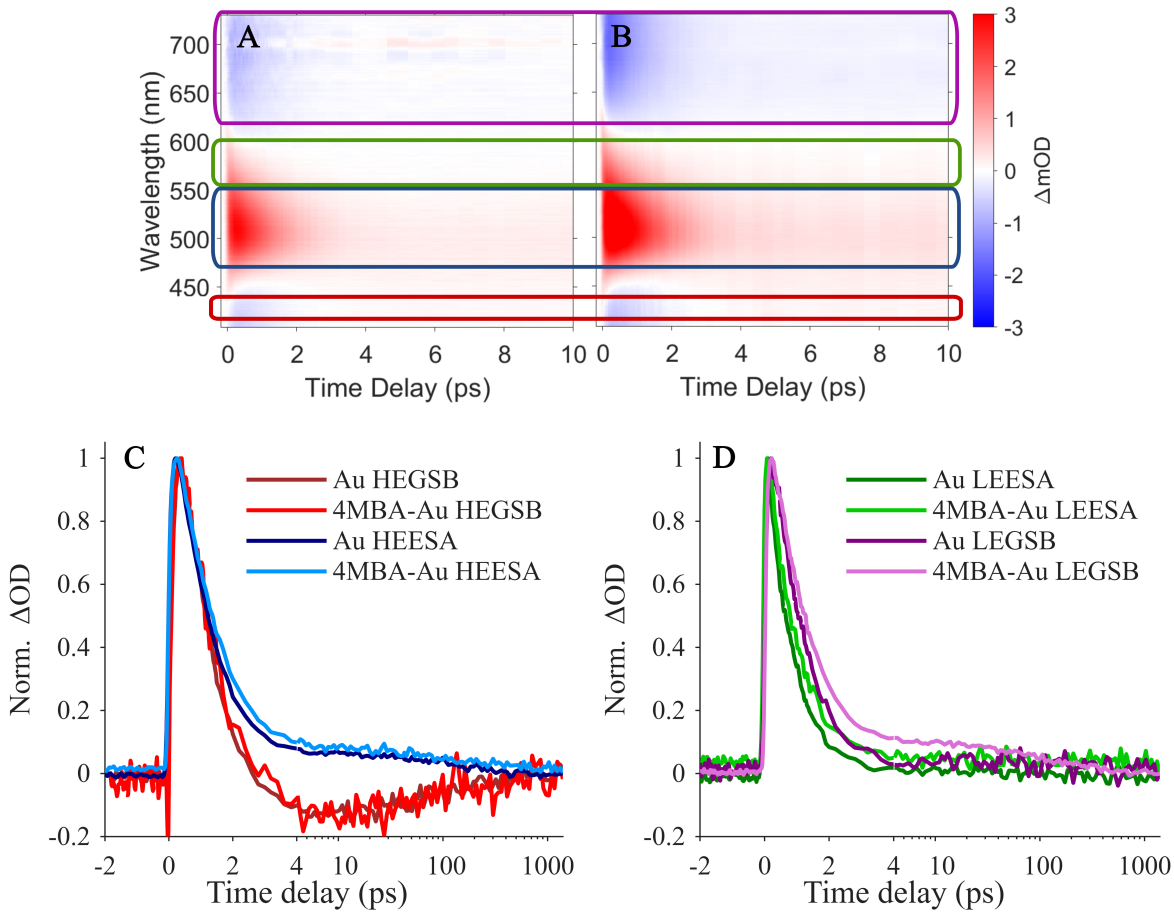

Figure S5: TA signal for A) Au and B) 4MBA-Au following 400 nm interband excitation. The spectral regions highlighted by red, blue, green, and purple represent HEGSB, HEESA, LEESA and LEGSB, respectively. Averaged and normalized TAS signal of C) HEGSB and HEESA and D) LEESA and LEGSB. The darker shades represent the signal from Au and the lighter shade represents the signal from 4MBA-Au. The time delay axis follows a linear scale upto 4 ps and a logarithmic scale afterwards.

TAS experiments with a 400 nm pump were performed on multiple pairs of Au and 4MBA-Au samples to test the reproducibility of the results. Figure S5 shows the TA signal and time traces at different energy regions for another pair of Au and 4MBA-Au. Similar to the observations in Figure 3, 4MBA-Au shows slower dynamics in the energy regions between 500 and 730 nm compared to Au. However, due to slight variations in film thickness and optical properties of Au between different sputter deposition runs, we refrain from averaging

the data collected across multiple pairs of samples.

S5. Global analysis of TAS data

Global target analysis of the TAS data was performed using the Glotaran software package [4] to simultaneously fit all wavelengths between 410-730 nm and obtain a fit that best describes the TA spectra. A kinetic model with a tri-exponential decay, convoluted with a Gaussian instrument response function, best follows the data and can be described by the following expression:

$$I(t) = \frac{1}{\sigma\sqrt{2\pi}} \exp\left(-\frac{(t-t_0)^2}{2\sigma^2}\right) * \sum_{i=1}^{3} A_i \exp\left(-\frac{(t-t_0)}{\tau_i}\right) \quad (1)$$

where t_0 is time zero, FWHM of the IRF is $\sigma\sqrt{8ln(2)}$, and A_i and τ_i are the amplitude and lifetimes, respectively. Figure S6 shows example experimental time traces and overall fit obtained by the global fit at a representative wavelength (520 nm). We obtained root mean square (RMS) values of 0.000042 and 0.000045 for Au and 4MBA-Au fits, respectively. These low RMS values indicate that the selected kinetic model adequately describes the TAS data.

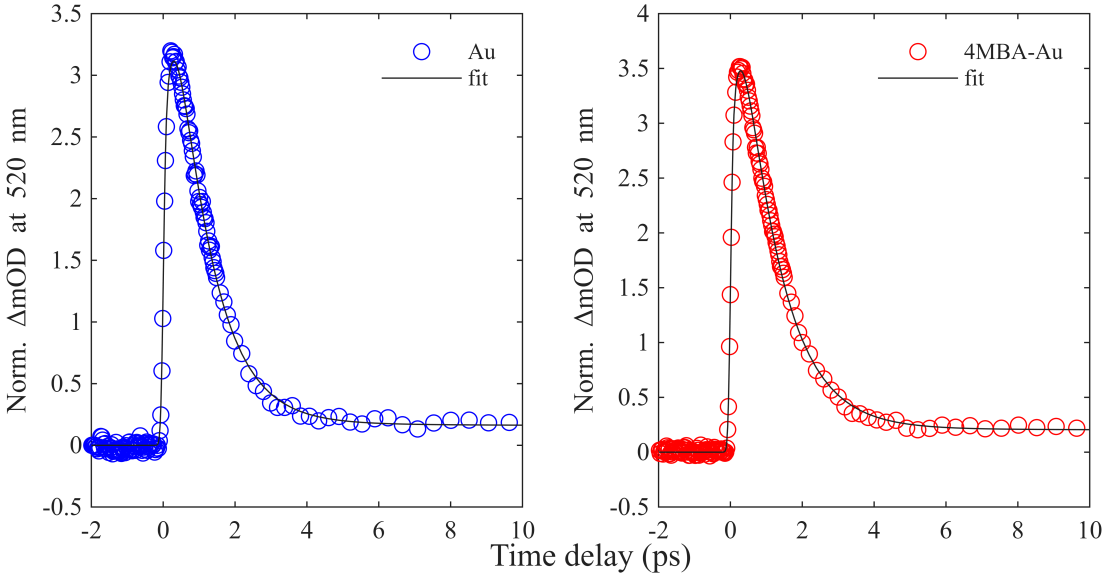

Figure S6: Fits (black) at 520 nm obtained from global fit analysis for Au (blue) and 4MBA-Au (red).

References

(1) Giannozzi, P.; Baroni, S.; Bonini, N.; Calandra, M.; Car, R.; Cavazzoni, C.; Ceresoli, D.; Chiarotti, G. L.; Cococcioni, M.; Dabo, I. et al. QUANTUM ESPRESSO: a modular and open-source software project for quantum simulations of materials. *Journal of Physics: Condensed Matter* **2009**, *21*, 395502, DOI: 10.1088/0953-8984/21/39/395502.

(2) Cooper, C. T.; Rodriguez, M.; Blair, S.; Shumaker-Parry, J. S. Mid-infrared localized plasmons through structural control of gold and silver nanocrescents. *J. Phys. Chem. C* **2015**, *119*, 11826–11832.

(3) Jia, Y.; Liu, D.; Wang, X.; Cheng, B.; Cheng, H. Dynamically modulating the mid-infrared localized surface plasmon resonance of Al-doped ZnO nanocrystals. *Materials Research Express* **2023**, *10*, 095001.

(4) Snellenburg, J. J.; Laptenok, S.; Seger, R.; Mullen, K. M.; Van Stokkum, I. H. Glotaran: A Java-based graphical user interface for the R package TIMP. *J. Stat. Softw.* **2012**, *49*, 1–22.